Micro-kinetic simulations of the catalytic decomposition of hydrazine on the Cu(111) surface†

Saeedeh S. Tafreshi,[a] Alberto Roldan[b] and Nora H. de Leeuw*[ab]

Hydrazine (N_2H_4) is produced at industrial scale from the partial oxidation of ammonia or urea. The hydrogen content (12.5 wt%) and price of hydrazine make it a good source of hydrogen fuel, which is also easily transportable in the hydrate form, thus enabling the production of H_2 in situ. N_2H_4 is currently used as a monopropellant thruster to control and adjust the orbits and altitudes of spacecrafts and satellites; with similar procedures applicable in new carbon-free technologies for power generators, e.g. proton-exchange membrane fuel cells. The N_2H_4 decomposition is usually catalysed by the expensive Ir/Al_2O_3 material, but a more affordable catalyst is needed to scale-up the process whilst retaining reaction control. Using a complementary range of computational tools, including newly developed micro-kinetic simulations, we have derived and analysed the N_2H_4 decomposition mechanism on the Cu(111) surface, where the energetic terms of all states have been corrected by entropic terms. The simulated temperature-programmed reactions have shown how the pre-adsorbed N_2H_4 coverage and heating rate affect the evolution of products, including NH_3, N_2 and H_2. The batch reactor simulations have revealed that for the scenario of an ideal Cu terrace, a slow but constant production of H_2 occurs, 5.4% at a temperature of 350 K, while the discharged NH_3 can be recycled into N_2H_4. These results show that Cu(111) is not suitable for hydrogen production from hydrazine. However, real catalysts are multi-faceted and present defects, where previous work has shown a more favourable N_2H_4 decomposition mechanism, and, perhaps, the decomposition of NH_3 improves the production of hydrogen. As such, further investigation is needed to develop a general picture.

1. Introduction

Hydrazine (N_2H_4) decomposition by heterogeneous catalysis is employed in a proton-exchange membrane fuel cell (PEMFC), due to its hydrogen content of 12.5 wt%. Moreover, since hydrazine hydrate is liquid under mild conditions and its

[a]Department of Chemistry, University College London, 20 Gordon Street, London, WC1H 0AJ, UK

[b]School of Chemistry, Cardiff University, Main Building, Park Place, Cardiff, CF10 3AT, UK. E-mail: DeLeeuwN@cardiff.ac.uk; Tel: +44 (0)2920870658

decomposition over catalysts at room temperature is exothermic without the need for added energy, it is ideal for portable applications such as space vehicles and satellites.[1–5] Hydrazine is also used in a monopropellant thruster to control and adjust the orbits and altitudes of spacecra s and satellites, based on the production of much larger volumes of nitrogen, hydrogen and ammonia gases from hydrazine.[2] The most important catalyst used in the hydrazine decomposition reaction is Ir/Al_2O_3 with a very high loading of iridium (20–40%).[2,6–8] However, owing to the high price and limited resources of iridium, considerable research has been focused on the devel-opment of active but cheaper and readily available alternative catalysts for hydrazine decomposition. Al-Haydari et al. showed that hydrazine molecules adsorb molecu-larly on a Cu lm at 243 K with 20% of the adsorption being reversible; further dissociative adsorption continues above 303 K, producing mainly NH_3 with N_2 and H_2 gaseous by-products.[9] As for the production of hydrogen, we aim to investigate the catalytic activity of Cu towards hydrazine decomposition for the production of hydrogen, and hinder the use of hydrocarbon steam reforming at industrial scale.[10]

Micro-kinetic simulations are convenient tools to approach a catalytic process from the atomic level to reactor conditions. In recent years, there has been increasing interest in the development of micro-kinetic models for various industrially relevant processes, such as ammonia synthesis,[11–14] oxidation,[15,16] and decomposition,[14,17] methanol synthesis[18] and decomposition,[19–21] ethylene oxidation[22], and the water gas shi reaction.[23–25] To construct a reliable micro-kinetic model, it is necessary to investigate all the relevant processes involved, such as adsorption, desorption, and surface reactions. Density functional theory (DFT) is commonly used to determine the energy pro le along the reaction pathway that will be employed in the micro-kinetic modelling.[26,27]

We have successfully investigated the dissociative adsorption of hydrazine (N_2H_4) on the planar and stepped Cu(111) surfaces by rst-principles calcula-tions,[28] where the thermodynamic and kinetic potential energy surface (PES) showed that intermolecular dehydrogenation of hydrazine to produce NH_3 and N_2 is the favoured route among the explored reaction network.[28] Based on the identi ed mechanism, we have established a micro-kinetic model to simulate a batch reactor where hydrazine is in contact with the planar Cu(111) surface, using 52 elementary reactions including adsorption, desorption, and reactions on the surface. We have evaluated the eff ects of temperature, initial N_2H_4 coverage and heating rate on a temperature-programmed reaction (TPR), as well as the selectivity towards the formation of NH_3, N_2, and H_2, resulting in an excellent agreement with the experimental results.

2. Computational methods

In the heterogeneous catalytic system, the constant rate of each surface elemen-tary step is commonly computed using the transition-state theory (TST) approx-imations of Eyring[29] and Evans and Polanyi.[30] Although TST is widely applicable and provides a useful description of the chemical reaction rates, it has limita-tions. For example, rather than surmount the reaction energy barrier, the reac-tants could quantum mechanically tunnel across the barrier, even though their energy is considerably less than the energy needed to go over the barrier. This could be important where the energy barrier is low, as the probability of tunnelling increases with a decreasing energy barrier.[31] TST also fails in its

description of reactions at high temperature, where the motion of molecules becomes more complex and collisions may lead to transition states far away from the lowest energy saddle point on the potential energy surface.[32] TST assumes that each intermediate is long-lived in each elementary step to reach a Boltzmann distribution of energy, and it thus fails in situations where intermediates are very short-lived.[33] TST also assumes that the transition states can evolve only to products, while in some cases they may return to the reactants. However, this theory still remains very useful in calculating the thermodynamic properties of the transition state and the reaction rates. More information about TST and rate constants is supplied in the ESI.†

Based on the mechanisms investigated in our previous work on the decom-position of N_2H_4 on the Cu(111) surface, the micro-kinetic model constitutes the 52 reactions summarized in Table 1. Following the approach of a previous study,[33] in this model, the lateral adsorbate–adsorbate interactions are negligible. Surface diffusion is also neglected, assuming that its energy barrier is much smaller than any reaction barrier in the decomposition process. Non-limiting mass transfer is also assumed.

Upon de ning the rate equations, we used numerical methods to solve the set of differential equations, which describe the relationship between the species coverages and time.

All of the thermodynamic and kinetic parameters were extracted from calcula-tions based on density functional theory (DFT)[34–36] using the VASP code.[37–40] The total energy calculations were performed using the Perdew–Burke–Ernzerhof (PBE)[41] form of the generalized gradient approximation (GGA), whereas the projector augmented wave (PAW) method was used to consider the effect of the inner cores on the valence density.[42,43] To improve the description of the long-range interactions, and following our previous work on the Cu–hydrazine system,[27] we employed the DFT-D2 method of Grimme as implemented in VASP,[44] which has been shown to improve accuracy on several systems.[27,34,45] Plane wave basis sets were used with an energy cut-off at 600 eV, which gave bulk energies converged to within 0.001 eV per atom. This high value for the cut-off energy ensured that no Pulay stresses occurred within the cell during relaxations. A 5 5 1 Monkhorst–Pack grid[46] of K-points was used to sample the Brillouin zone for surfaces. The slabs were modelled with a 2 2 supercell, p(4 4), with an area of 88.37 A^2 and a vacuum layer of 20 A between slabs. The adsorbate and the top three out of four layers of the slabs were allowed to relax during structural optimisation, in line with previous studies.[47,48] Different slab thicknesses were tested until convergence was achieved.

A combination of two techniques were used to identify transition state (TS) structures: the climbing image nudged elastic band (NEB) method[49,50] and the improved dimer method (IDM),[51] which we veri ed by a single imaginary frequency associated with the reaction coordinate.

We have calculated the adsorption (E_{ads}) and desorption (E_{des} ¼ E_{ads}) ener-gies for the species using eqn (1);

$$E_{ads} ¼ E_{molecule}^{surf} \quad (E^{surf} + E_{molecule}^{gas}) \tag{1}$$

where $E^{surf}_{molecule}$ is the total energy of the species adsorbed on a relaxed Cu(111) surface, and E^{surf} and $E^{gas}_{molecule}$ are the energies of the naked surface and isolated gas-phase molecules, respectively. Within this de nition, a negative E_{ads} value

Table 1 Calculated ZPE corrected reaction (E^{ZPE}_r) and barrier (E^{ZPE}_a) energies for the reaction pathways considered. The pre-exponential factors (A_0) and reaction rate constants (k) at 300 and 650 K are also included. The E^{ZPE}_r of the adsorption and desorption processes are the corresponding E^{ZPE}_{ads} and E^{ZPE}_{des}, which for each species were calculated relative to the gas-phase species. Note that "*" and (X*) indicate a free site and the adsorbed species on the surface, respectively. The units of A_0 and k for first order and second order reactions are s^{-1} and $ML^{-1}\ s^{-1}$, respectively

	Reactions	E_r^{ZPE} (eV)	E_a^{ZPE} (eV)	A_0 300 K	A_0 650 K	k 300 K	k 650 K
Adsorption–desorption							
R0	N_2H_4 þ */N_2H_4*	0.94	—	1.04 10^4	7.06 10^3	1.21 10^2	4.91 10^4
	*/ *	0.94	—	2.31	1.75	5.33	2.71
R1	N_2H_4 N_2H_4 þ			10^{11}	10^{10}	10^4	10^{11} 10^{10}
	*/ *	0.78	—	4.98	9.19	2.01	9.10
R2	NH_3 NH_3 þ			10^{11}	10^{10}	10^8	10^{11} 10^{10}
	*/ *		—	1.43	9.69	2.68	7.15
R3	NH_3 þ NH_3	0.78		10^4	10^3		10^2
	*/ *	0.11	—	6.72	6.93	8.26	8.10
R4	N_2 N_2 þ			10^{10}	10^9	10^{12}	10^{13} 10^{10}
R5	N_2 þ */N_2*	0.11	—	1.11 10^4	7.55 10^3	6.10 10^1	8.83 10^2
R6	H* + H* / H + 2*	0.45	1.08	5.81	6.01	1.04	1.02
	2			10^{12}	10^{12}	10^8	10^{14} 10^{10}
R7	H + 2* / H* + H*	0.45	0.65	4.16	2.82	9.83	1.42
	2			10^4	10^4	10^2	10^2
N_2H_x (x ¼ 1–4) dehydrogenation							
R8	N_2H_4*/N_2H_3* þ H*	0.16	1.30	8.33 10^{12}	2.14 10^{13}	1.30 10^9	2.54 10^3
R9	N_2H_3* þ H*/N_2H_4*	0.16	1.14	3.12 10^{13}	1.06 10^{14}	6.13 10^6	9.15 10^5
R10	N_2H_3*/NNH_2* þ H*	0.55	1.26	2.54 10^{13}	1.14 10^{14}	8.37 10^8	1.78 10^5
R11	NNH * H*/N H *	0.55	0.71	1.45	6.00	1.23	2.84
	2 þ 2 3			10^{13}	10^{13}	10^7	10^{11} 10^{10}
R12	N_2H_3*/NHNH* þ H*	0.64	1.35	1.47 10^{13}	4.26 10^{13}	7.84 10^{10}	4.75 10^3
R13	NHNH* H*/N H *	0.64	0.71	5.52	9.61	4.74	1.95
	þ 2 3			10^{12}	10^{12}		10^7
R14	NNH_2*/NNH* þ H*	0.45	1.12	9.77 10^{12}	2.12 10^{13}	2.46 10^6	7.04 10^4
R15	NNH* H*/NNH *	0.45	0.67	1.81	6.00	8.64	2.35
	þ 2			10^{13}	10^{13}	10^4	10^{10} 10^{10}
R16	NHNH* / NNH* + H*	0.46	1.47	2.03 10^{13}	4.88 10^{13}	3.3 10^5	6.33 10^5
R17	NNH* + H* / NHNH*	0.46	1.01	1.75	4.51	8.12	4.60
				10^{13}	10^{13}	10^3	10^9

Table 1 (Contd.)

	Reactions	E_r^{ZPE} (eV)	E_a^{ZPE} (eV)	A_0 300 K	A_0 650 K	k 300 K	k 650 K
R18	NNH*/N * H*	1.62	0.17	1.54	4.16	4.64	5.81
	2 þ			10^{13}	10^{13}	10^{10}	10^{12}
R19	N_2* þ H*/NNH*	1.62	1.79	2.13	3.51	9.17	1.44
				10^{12}	10^{12}	10^{19}	10^{2}
	N_2H_x (x ¼ 1–4) N–N decoupling						
R20	N H */NH * NH *	0.98	0.69	1.68	5.74	1.22	1.11
	2 4 2 þ 2			10^{13}	10^{13}	10^{2}	10^{9}
R21	NH_2* þ NH_2*/N_2H_4*	0.98	1.67	3.72	8.93	1.90	6.54
				10^{13}	10^{13}	10^{14}	10
R22	N_2H_3*/NH_2* þ NH*	0.39	0.90	1.10	3.54	9.1	7.86
				10^{13}	10^{13}	10^{3}	10^{6}
R23	NH_2* þ NH*/N_2H_3*	0.39	1.29	1.17	2.59	3.68	4.40
				10^{13}	10^{13}	10^{9}	10^{3}
R24	NNH_2*/NH_2* þ N*	0.12	1.35	2.87	4.42	3.58	5.54
				10^{12}	10^{12}	10^{11}	10
R25	NH_2* þ N*/NNH_2*	0.12	1.23	1.40	3.64	1.07	3.48
				10^{13}	10^{13}	10^{7}	10^{4}
R26	NHNH* / NH* + NH*	0.38	0.79	2.42	3.05	9.97	7.09
				10^{12}	10^{12}	10^{2}	10^{5}
R27	NH* + NH* / NHNH*	0.38	1.17	8.86	1.43	6.14	1.86
				10^{12}	10^{13}	10^{7}	10^{4}
R28	NNH* / NH* + N*	0.15	1.42	1.47	1.62	4.48	1.83
				10^{12}	10^{12}	10^{13}	
R29	NH* + N* / NNH*	0.15	1.27	7.53	1.28	4.08	1.69
				10^{12}	10^{13}	10^{9}	10^{3}
	NH_x (x ¼ 1–3) dehydrogenation						
R30	NH_3*/NH_2* þ H*	0.60	1.41	3.26	9.05	3.27	6.85
				10^{12}	10^{12}	10^{12}	10
R31	NH_2* þ H*/NH_3*	0.60	0.81	1.04	2.57	6.00	2.99
				10^{13}	10^{13}	10^{1}	10^{7}
R32	NH_2*/NH* þ H*	0.56	1.40	3.12	4.64	6.60	1.52
				10^{12}	10^{12}	10^{6}	10^{4}
R33	NH* þ H*/NH_2*	0.56	0.84	1.08	2.99	2.14	2.43
				10^{13}	10^{13}	10^{1}	10^{7}
R34	NH* / N* + H*	1.34	1.79	6.31	1.22	5.16	1.70
				10^{12}	10^{13}	10^{20}	10^{2}
R35	N* + H* / NH*	1.34	0.45	6.89	1.44	2.62	6.53
				10^{12}	10^{13}	10^{3}	10^{8}
	Interaction of NH_2 molecules						
R36	2NH */NH* NH *	0.00	0.45	1.54	2.58	1.08	4.69
	2 þ 3			10^{13}	10^{13}	10^{7}	10^{10}
R37	NH* NH */2NH *	0.00	0.45	1.19	2.88	6.20	1.97
	þ 3 2			10^{13}	10^{13}	10^{5}	10^{10}

Table 1 (Contd.)

Reactions	E_{rZPE} (eV)	E_{aZPE} (eV)	A_0 300 K	A_0 650 K	k 300 K	k 650 K
Interaction of NH_2 with N_2H_x (x ¼ 1–4)						
* */ * *			2.42	2.73	4.81	2.38
R38 N_2H_4 þ NH_2 N_2H_3 þ NH_3	0.36	0.42	10^{12}	10^{12}	10^{4}	10^{8}
R39 N_2H_3* þ NH_3*/N_2H_4* þ NH_2*	0.36	0.78	2.72	4.52	3.17	8.22
			10^{12}	10^{12}	10^{2}	10^{5}
* */ * *			5.64	9.39	1.10	7.79
R40 N_2H_3 þ NH_2 NHNH þ NH_3	0.08	0.64	10^{12}	10^{12}	10^{2}	10^{7}
* */ * *			1.04	8.98	3.73	2.06
R41 NHNH þ NH_3 N_2H_3 þ NH_2	0.08	0.56	10^{12}	10^{11}	10	10^{6}
* */ * *			1.37	3.14	5.58	2.35
R42 N_2H_3 þ NH_2 NNH_2 þ NH_3	0.13	0.53	10^{13}	10^{13}	10^{3}	10^{9}
* */ * *			1.98	2.46	5.18	3.44
R43 NNH_2 þ NH_3 N_2H_3 þ NH_2	0.13	0.66	10^{12}	10^{12}		10^{6}
* */ * *			1.53	2.39	2.11	4.60
R44 NHNH þ NH_2 NNH þ NH_3	0.23	0.25	10^{13}	10^{13}	10^{9}	10^{11}
R45 NNH* NH */NHNH* NH *			4.44	5.50	2.41	10^{10} 4.00
R46 NNH * þ 3 NH */NNH* þ 2 NH *	0.23	0.48	10^{12}	10^{12}	10^{4}	10^{8}
			2.55	5.38	1.05	1.06
2 þ 2 þ 3	0.12	0.30	10^{13}	10^{13}	10^{9}	10^{12}
R47 NNH* */ * *			7.72	1.60	1.21	10^{10} 8.63
þ NH_3 NNH_2 þ NH_2	0.12	0.18	10^{12}	10^{13}	10^{10}	10^{11}
R48 NNH* NH */N * NH *			1.60	3.11	4.38	10^{10} 2.54
þ 2 2 þ 3	2.09	0.08	10^{13}	10^{13}	10^{12}	10^{13}
R49 N_2* þ NH_3*/NNH* þ NH_2*	2.09	2.17	1.00	1.43	1.25	10^{10} 3.26
			10^{12}	10^{12}	10^{25}	
						10^{6}
N_2 dissociation						
R50 N_2*/N* þ N*	3.20	4.69	6.71	7.03	1.09	1.53
			10^{11}	10^{11}	10^{68}	
						10^{26}
R51 N* þ N*/N_2*	3.20	1.49	3.01	9.02	1.08	1.51
			10^{13}	10^{13}	10^{11}	10^{3}

means a release of energy during adsorption. The reaction energies (E_r) were estimated by the difference in energy between the nal and initial states; hence, a negative E_r indicates an exothermic process. The forward activation barrier (E_a) was de ned as the energy difference between the transition state (TS) and the initial state. We have also considered the effect of temperature on E_{ads}, E_r and E_a; see the ESI for details.†

3. Results and discussion

The 52 elementary steps for hydrazine decomposition summarised in Table 1 include the adsorption and desorption of reactants and products, N–N

decoupling, dehydrogenation of N_2H_x (x ¼ 1–4) and NH_x (x ¼ 1–3), and intermolecular interactions on the surface. We have also included in Table 1 the reaction (E^{ZPE}_r) and barrier (E^{ZPE}_a) corrected with the zero-point energy, the pre-exponential factors (A_0), and the reaction rate constants (k) of each elementary step at 300 and 650 K. We have represented the reaction rate constants as a function of the temperature in Fig. S3 of the ESI.† Calculation of the reaction rate constants help us to determine the reaction rate as a function of the temperature, from which we can conclude which step is the rate-limiting reaction. The adsorption sticking coefficients (S_0) of N_2H_4, NH_3, N_2, and H_2 on the Cu(111) surface at 300 and 650 K are also provided in Table 2, where similar results have been reported for NH_3 on Ru(0001),[52] N_2 on Fe(100) and Fe(111)[53], and H_2 on low-index Cu surfaces.[54] We have calculated two different microkinetic models. In the rst part of our work, we have modelled a temperature-programmed reaction (TPR) where, starting from pre-adsorbed N_2H_4, the temperature increased at different rates from 100 to 500 K, while any gas was extracted to avoid the re-adsorption of gases (R0, R3, R5 and R7). In the second section, we have explored the catalytic activity of copper surfaces towards N_2H_4 dissociation in a batch reactor under varying conditions, starting from a situation where the naked Cu surface is in contact with a given pressure of N_2H_4. The rate equations of the elementary reactions and corresponding differential equations are listed in the ESI.†

3.1. Temperature programmed reaction simulation

Fig. 1 shows the simulated TPR spectra of N_2H_4, NH_3, N_2 and H_2 gases from different initial N_2H_4 coverages. The TPR plots show desorption of species from the surface as the temperature increases. The desorption peaks therefore show the temperature at which the molecules have the highest desorption rate. As Fig. 1 shows, different initial N_2H_4 coverages do not change the temperature of the maximum desorption rate. Fig. 1 in conjunction with Fig. 2 relates the pressures of desorbed gases and the coverages of the most abundant species on the surface, i.e. N_2H_4, N_2H_3 and NH, as a function of temperature. Fig. 1a indicates that N_2H_4 desorption takes place at around 213 K, similarly to the desorption peak on a Rh foil surface.[55] As Fig. 2b shows, N_2H_4 disappears completely from the surface at around 220 K by desorbing or converting to species such as N_2H_3 and NH_3, which

Table 2 Calculated sticking coefficients (S_0) of N_2H_4, NH_3, N_2, and H_2 adsorption on the Cu(111) surface at 300 and 650 K. Note that "*" and (X*) indicate a free site and the adsorbed species on the surface, respectively

	Reactions	S_0 this work, 300 K	S_0 this work, 650 K	S_0 other works
R0	N_2H_4 þ */N_2H_4*	1.17 10 6	6.96 10 8	—
R3	NH_3 þ */NH_3*	1.88 10 4	7.38 10 6	#2 10 4, 300–500 K (ref. 52)
R5	N_2 þ */N_2*	5.5 10 5	1.2 10 5	1.0 10 6 to 1.0 10 7, 500 K (ref. 53)
R7	H_2 + * / 2H*	2.36 10 2	5.03 10 3	1.0 10 5 to 5.0 10 2, 190 K (ref. 54)

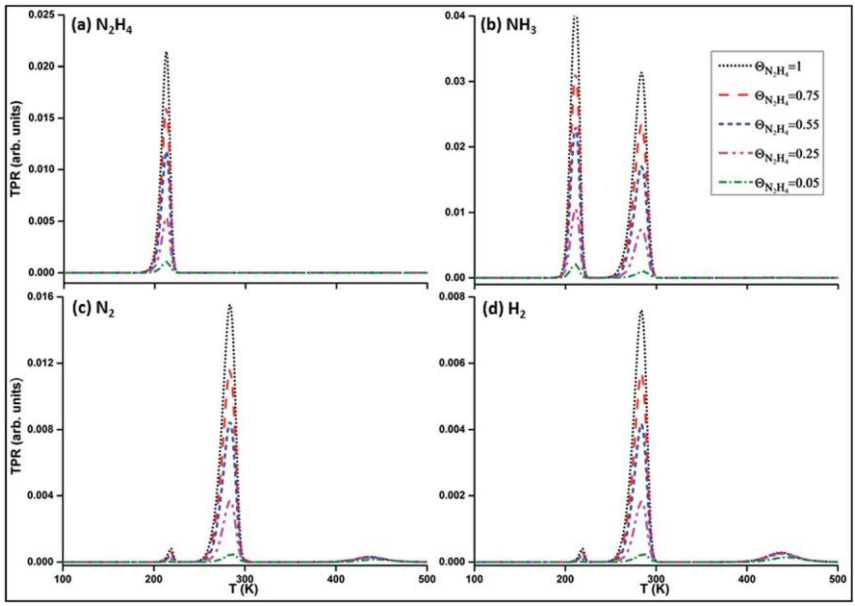

Fig. 1 Simulated TPR spectra for N_2H_4, NH_3, N_2, and H_2 desorption from the Cu(111) surface, starting from adsorbed N_2H_4 at different initial coverages at a reaction time of 1 s with a 1 K min^{-1} heating rate.

desorb quickly from the surface (k_2 10^8 s^{-1}). NH_3 starts to desorb at around 190 K which agrees well with the results of the thermal desorption spectroscopy (TDS) study of NH_3 adsorption on Cu(100), where it desorbs at 185 10 K.[56] The high amount of N_2H_3 on the surface between 200–300 K (Fig. 2b) and NH_3 desorbed from the surface, i.e. the rst peak of the NH_3 TPR at 211 K (Fig. 1b), indicate that an inter-molecular dehydrogenation mechanism is taking place. N_2H_4 produces NH_2 from N–N decoupling (R38), which, at this low temperature, is feasible from kinetic and thermodynamic points of view. This reaction is the most favoured step in the temperature range of 200–265 K, where the N_2H_3 coverage increases.

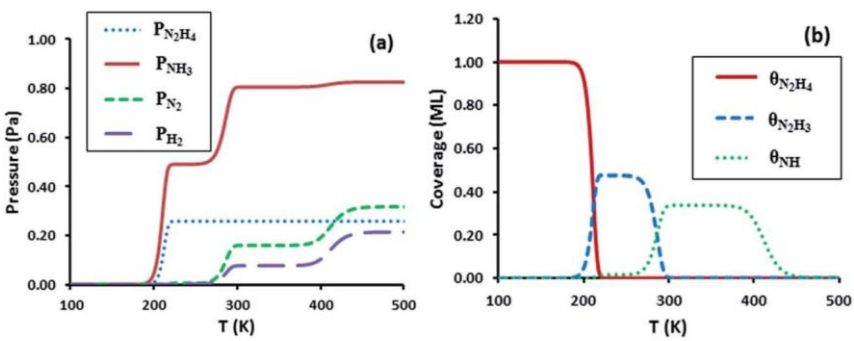

Fig. 2 (a) The partial pressure of desorbed N_2H_4, NH_3, N_2 and H_2 gases and (b) surface coverage of N_2H_4, N_2H_3 and NH as a function of temperature with an initial N_2H_4 full coverage in the TPR simulation at a reaction time of 1 s with a 1 K min^{-1} heating rate.

However, at higher temperatures, the N_2H_3 coverage decreases by reacting with NH_2 intermediates, losing hydrogen atoms (R40, R42, R44, R46 and R48) and resulting in the formation of other species, i.e. the NH_3 peak at 284 K (Fig. 1b).

The N_2 and H_2 have three desorption peaks, two smaller peaks at around 219 and 440 K and a maximum desorption peak at 284 K. The N_2 and H_2 desorption peaks at 219 K are due to the recombination of H and N ad-atoms on the surface, produced by the decomposition of intermediates. The produced N_2 and H_2 desorb from the surface due to the small desorption energies of 0.11 and 0.45 eV, respectively, which are in agreement with measurements on single crystals and polycrystalline Cu, where the heat of adsorption of N_2 on Cu(110) was determined to be 0.088 eV using helium scattering,[57] while the adsorption energy of H_2 lies between 0.39 and 0.48 eV on various forms of unsupported Cu.[54,58–64] The maximum N_2 and H_2 desorption peaks at around 284 K, which appear at the same temperature as the second NH_3 desorption peak, are due to reactions of inter-molecular dehydrogenation, resulting in the production of NNH. This leads to the reaction between NNH and NH_2 (R48), as well as NNH decomposition (R18). The smaller peaks at higher temperatures correspond to the recombination of atomic H and N following the decomposition reactions of NH to N and H on the surface (R34). NH is stable on the surface until 450 K, as shown in Fig. 2b, in line with other studies of hydrazine dissociation on Ni[65] and Rh.[66]

Fig. 3 shows the spectra of the gases produced during the TPR, at an initial condition of full coverage of N_2H_4, for a temperature range from 100 to 600 K and with three heating rates of 1, 5 and 8 K min^{-1}. As the heating rate increases, so does the temperature at which the desorption rate is at its maximum (peak

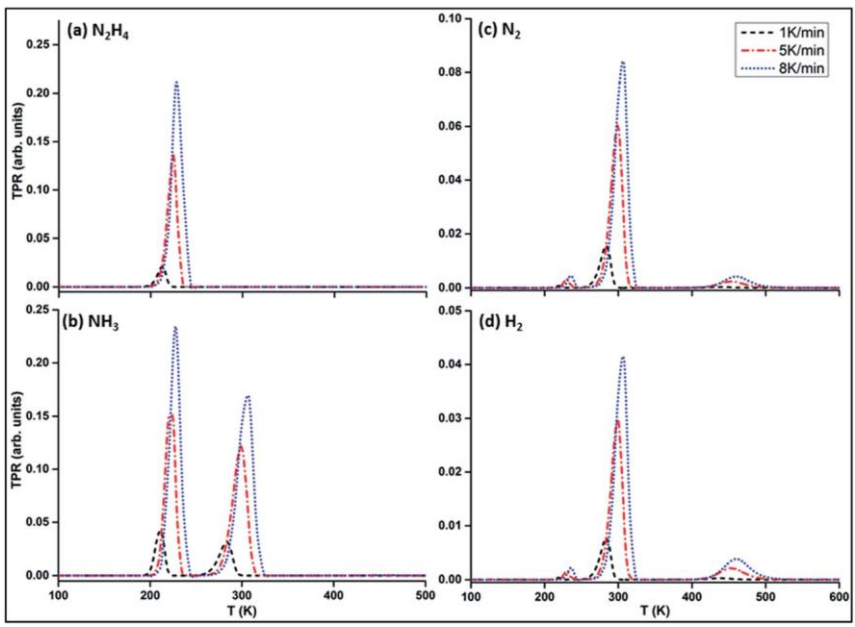

Fig. 3 Simulated TPR curves for N_2H_4, NH_3, N_2 and H_2 desorption from the Cu(111) surface, starting from an initial N_2H_4 coverage of 1 ML (full coverage) at a reaction time of 1 s for different heating rates.

temperature), whereas the intensity of the peak increases as well, in agreement with an experimental TPR study of hydrazine decomposition on an Al_2O_3-sup-ported Ir catalyst.[67] These changes in peak temperature and intensity are related to a sudden variation of the pressures and the derivative slope. The higher the heating rate, the more abrupt are the changes in pressure and the higher the slope of $\frac{dP}{dT}$. Note that the abrupt desorption of N_2H_4 reduces the time for further reaction on the surface to produce NH_3, N_2 and H_2, indicating that a slower heating rate helps to increase the yield of NH_3, N_2 and H_2, Fig. 4.

The composition of the exhaled gas resulting from the hydrazine interaction with the Cu(111) surface at different temperatures is given in Table 3 and is in agreement with the experimental report by Al-Haydari et al.[9] NH_3 is the main gaseous product of hydrazine decomposition, whereas H_2 is the least present. According to the experiment, the temperature at which hydrazine starts to decompose is 303 K when NH_3, N_2 and some H_2 desorb from the Cu lm.[9] In our simulation, as shown in Fig. 3, hydrazine starts to decompose at 190 K, when the rst NH_3 can be observed, while N_2 and H_2 desorb at a higher temperature of 219 K. This discrepancy between the experiment and simulation may be due to the adsorption of gases into the liquid hydrazine, as well as the use of a Cu lm without a well-de ned Cu structure, which may include defects. Our previous works have shown that the introduction of defects on the surface provides more favourable sites for stronger hydrazine adsorption, resulting in higher tempera-tures for decomposition and desorption.[34,35] Moreover, the heating rate and the reaction time of the experimental study were not reported.

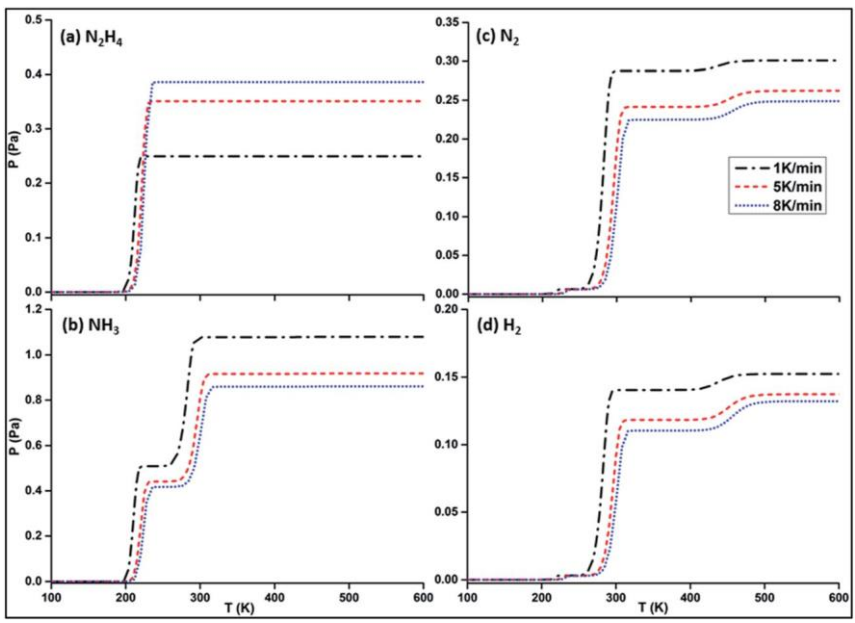

Fig. 4 N_2H_4, NH_3, N_2 and H_2 evolution from Cu(111) surface as a function of temperature for an initial N_2H_4 coverage of 1 ML (full coverage) in the TPR simulation at a reaction time of 1 s for different heating rates.

Table 3 Percentage composition of gaseous products throughout hydrazine decom-position on the Cu(111) surface from the initial N_2H_4 full coverage in the TPR simulation at a reaction time of 1 s with a 1 K min ^{1} heating rate at different temperatures, in comparison with experimental reports[9]

	NH_3 (%)		N_2 (%)		H_2 (%)	
T (K)	This work	Ref. 9	This work	Ref. 9	This work	Ref. 9
303	77.28	75.60	15.33	18.75	7.38	5.62
333	77.28	72.63	15.34	22.93	7.39	4.58
363	77.23	69.49	15.36	27.23	7.41	3.25
393	75.25	69.56	16.37	27.34	8.38	3.10

3.2. Batch reactor simulation

The micro-kinetic simulation of a batch reactor, discussed in this section, considers all elementary steps in Table 1 and starts from a situation where the naked Cu surface is exposed to N_2H_4 gas. We have carried out the micro-kinetic simulations of hydrazine decomposition at a small initial N_2H_4 pressure of 6 Pa in

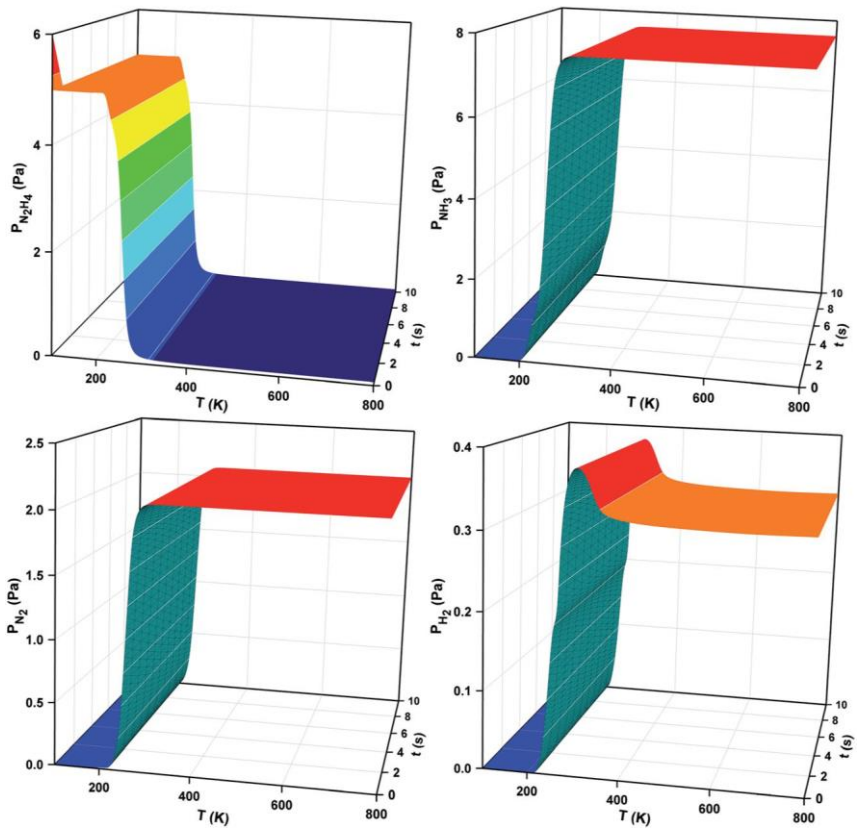

Fig. 5 N_2H_4, NH_3, N_2 and H_2 evolution from the Cu(111) surface as a function of temperature and time for an initial N_2H_4 pressure of 6 Pa with a 1 K min ^{1} heating rate in the batch reactor simulation.

the temperature range of 100–800 K. The corresponding differential equations are listed in the ESI.†

We have represented the pressure of N_2H_4, NH_3, N_2 and H_2 as a function of the temperature and the reaction time in 3D plots (Fig. 5). They show that at 100 K N_2H_4 reaches full coverage of the exposed surface. The decomposition of the N_2H_4 molecules on the surface starts at around 200 K and the N_2H_4 molecules still in the gas phase can occupy the resulting empty sites on the surface. N_2H_4 pressure reaches an equilibrium state at around 300 K, when its pressure decreases below 0.1 Pa. The NH_3 starts to desorb from the Cu(111) surface at around 200 K, while N_2 and H_2 appear in the gas phase at the higher temperature of 220 K. NH_3 and N_2 desorption reach equilibrium at around 300 K, with pressures of 7.5 and 2.1 Pa respectively, and any increase in the temperature does not further affect their desorption. The H_2 pressure increases with increasing temperature up to 300 K (0.38 Pa), and then decreases to 0.33 Pa at 370 K, due to the adsorption and reaction with N ad-atoms producing NH_3.

To understand the N_2H_4 overall decomposition mechanisms, the coverage of some prominent intermediates is plotted in Fig. 6 showing how the coverages of N_2H_4, N_2H_3, NH_3, H and NH change with temperature at 1 s a er the surface was covered fully with adsorbed N_2H_4.

The observed trends for the coverages of N_2H_4, N_2H_3 and NH in the batch reactor simulation are the same as those in the TPR simulation, although the coverages of the species are different owing to the adsorption of species on the surface. The hydrazine N–N decoupling (R20) is again the most preferred reaction mechanism among the ones studied due to a relatively low energy barrier. The produced NH_2 intermediate subtracts one of the hydrogens of a co-adsorbed hydrazine molecule, resulting in the production of NH_3 and N_2H_3 molecules on the Cu(111) surface (R38), which is an exothermic reaction (E_r ¼ 0.36 eV) with a relatively low energy barrier of 0.42 eV. Fig. 6a shows that as soon as the coverage of N_2H_4 molecules on the surface starts to decrease, the coverage of the N_2H_3 intermediate increases until all N_2H_4 is converted to N_2H_3 and NH_3 at 230 K, when almost the entire surface is covered with N_2H_3 and some NH_3 molecules. The coverage of NH_3, Fig. 6b, decreases quickly when the temperature reaches 215 K due to a relatively small desorption energy of 0.78 eV, which compares well with the experimental desorption energy on Cu(001) of 0.72 0.07 eV.[56] N_2H_3 is stable

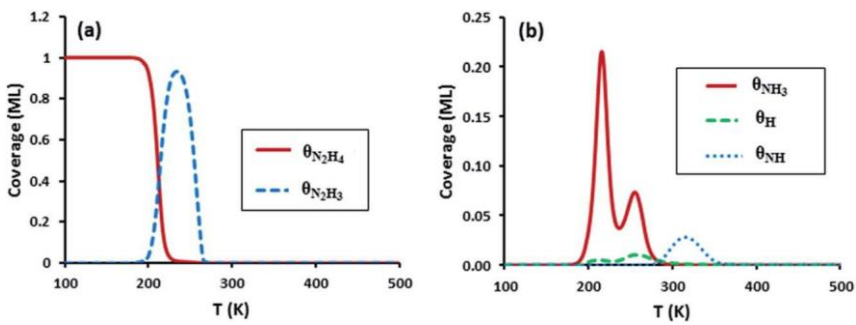

Fig. 6 The surface coverage of (a) N_2H_4 and N_2H_3, (b) NH_3, H and NH as a function of temperature with an initial N_2H_4 pressure of 6 Pa, in the batch reactor simulation at a reaction time of 1 s with a 1 K min^{-1} heating rate.

on the surface in the temperature range of 190–265 K and NH_3 has obtained enough energy to desorb from the surface. The NH_2 present on the surface, ob-tained from the $H_2N–NH_2$ bond breaking, reacts with N_2H_3 (R40 and R42) in an intermolecular dehydrogenation mechanism, causing a decrease in the N_2H_3 coverage at around 230 K and also leading to other species on the surface.

The existence of H atoms on the surface in the temperature range of 200–350 K (Fig. 6b) indicates the dehydrogenation of adsorbed species with energy barriers higher than 1.2 eV (R8, R10, R12, R14 and R16). The production of NH from the dehydrogenation of NH_3 and NH_2 on the surface (R30 and R32) takes place at temperatures higher than 270 K, because of an even higher energy barrier of 1.40 eV, which results in the observed NH peak in Fig. 6b centred at 315 K. From here, the NH coverage starts to decrease via decomposition to N and H atoms on the surface (R34), with an energy barrier of 1.79 eV. The fact that NH is stable in the temperature range of 270–370 K is in line with the experimental work by Gland et al., where they showed that NH is stable during hydrazine decomposition until 365 K on Ni(111)[65] as well as on Ru,[68] Rh,[66,69] Ir,[70] W,[71] and Mo[72] surfaces.

The associative desorption of hydrogen, produced by dehydrogenation, results in the peak centred at 300 K, shown in Fig. 5. The highly endothermic reaction between N_2 and H on the surface (R19), with an energy barrier of 1.79 eV, could only occur at high temperatures, and leads to a decrease of H_2 pressure at around 300 K, shown in Fig. 5, due to dissociative adsorption of H_2 in order to provide enough H atoms on the surface.

We have also examined the N_2H_4 conversion and NH_3, N_2 and H_2 selectivities at a xed temperature of 350 K as a function of the initial N_2H_4 pressure, varied from 10^{6} to 100 Pa, shown in Fig. 7a. The system reaches the highest NH_3 selectivity of 81.9% for an initial N_2H_4 pressure of 0.1 Pa, the N_2 selectivity reaches its maximum (36.3%) at $P_{N_2H_4}$ ¼ 100 Pa, and the maximum H_2 selectivity (5.4%) occurs for an initial N_2H_4 pressure of 0.001 Pa. N_2H_4 conversion is complete for $P_{N_2H_4}$ # 10 Pa.

Fig. 7b plots the N_2H_4 conversion and NH_3, N_2 and H_2 selectivities with temperature. The N_2H_4 conversion reaches its maximum at 330 K (98.5%), while NH_3, N_2 and H_2 selectivities converge to 64.5%, 35.1% and 2.6%, respectively, at 265 K.

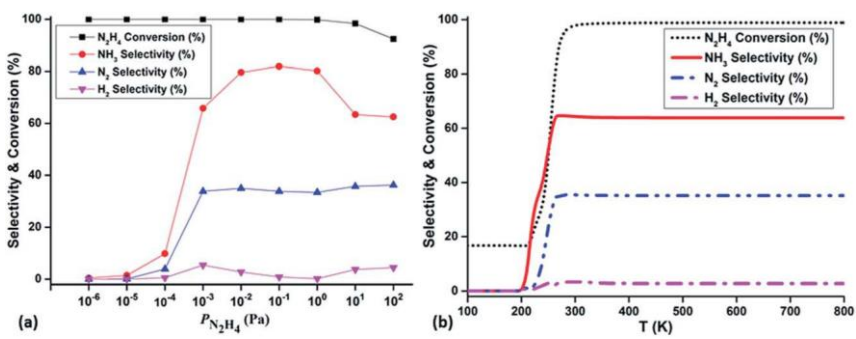

Fig. 7 N_2H_4 conversion and NH_3, N_2 and H_2 selectivities as a function of (a) initial N_2H_4 pressure at 350 K, (b) temperature with an initial N_2H_4 pressure of 6 Pa in the batch reactor simulation at a reaction time of 1 s with a 1 K min^{1} heating rate.

4. Conclusions

A micro-kinetic model based on results from density functional theory calcula-tions was established, taking into account adsorption, desorption and reaction processes of reactants, intermediates and products, involved in the N_2H_4 decomposition on the Cu(111) surface. Two simulation models have been considered; the rst model started from a situation of pre-adsorbed N_2H_4 and considered the constant removal of gases from the reactor, i.e. simulating TPR spectra. In the second model, we have considered the naked Cu(111) surface in contact with N_2H_4, where all the gaseous products from the N_2H_4 decomposition are allowed to adsorb and desorb freely until the system reaches equilibrium in the batch reactor. The simulated TPR shows gas desorption peaks depending on the heating rate and the initial N_2H_4 coverage. The simulations of the batch reactor show NH_3 being the major gaseous product on the extended surfaces, in agreement with experiments. The representation of the coverages of the inter-mediates with temperature shows that N_2H_3 and NH are the most stable inter-mediates on the surface during N_2H_4 decomposition in the 190–265 and 270–370 K temperature ranges, respectively. Temperature and initial N_2H_4 pressures affect the N_2H_4 conversion and the NH_3, N_2 and H_2 selectivities. The highest NH_3, N_2 and H_2 selectivities obtained in the simulation at 350 K are 81.9%, 36.3% and 5.4%, respectively, while an initial N_2H_4 pressure of 6 Pa gives a conversion of 98.5% at 330 K with NH_3, N_2 and H_2 selectivities of 64.5%, 35.1% and 2.6%, respectively. These results show that Cu(111) is not suitable for hydrogen production from hydrazine, as the dominant product is ammonia. It is known, however, that low coordinated metals are more active and may stabilise inter-mediates favouring the NH_3 decomposition pathway and therefore increase the production of H_2. Future studies of N_2H_4 decomposition processes on surfaces such as the (001) and (011), and on common defects, e.g. steps, will provide a general picture of the feasible production of H_2 from a cheap compound such as N_2H_3 on an abundant Cu catalyst. This study, whose ndings are in line with available experiments, validates the proposed mechanisms and shows that micro-kinetic simulations are an effective tool to predict yields and selectivities from DFT results under a wide range of temperature and pressure conditions. This method can now be further rolled out to alternative systems, including metal and non-metal systems.

Acknowledgements

S. S. T acknowledges University College London and the UCL Industrial Doctorate Centre in Molecular Modelling and Material Science for an Overseas Research Scholarship. N. H. d. L. acknowledges the Royal Society for an Industry Fellowship and A. R. is grateful to the Ramsay Memorial Trust and University College London for the award of a Ramsay Fellowship. Via our membership of the UK's HPC Materials Chemistry Consortium, which is funded by EPSRC (EP/L000202), this work made use of the facilities of HECToR and ARCHER, the UK's national high-performance computing service, which is funded by the Office of Science and Technology through EPSRC's High End Computing Programme, as well as the UCL Legion High Performance Computing facility (Legion@UCL), and associated support services.

References

1 M. Y. Zheng, R. H. Cheng, X. W. Chen, N. Li, L. Li, X. D. Wang and T. Zhang, Int. J. Hydrogen Energy, 2005, 30, 1081–1089.
2 E. W. Schmidt, Hydrazine and Its Derivatives: Preparation, Properties, Applications, Wiley, New York, 2nd edn, 2001.
3 S. G. Pakdehi, M. Salimi and M. Rasoolzadeh, Researches and Applications in Mechanical Engineering, 2014, 3, 21–25.
4 J. Block and G. Schulzek, J. Catal., 1973, 30, 327–329.
5 M. Grunze, Surf. Sci., 1979, 81, 603–625.
6 S. Mary, C. Kappenstein, S. Balcon, S. Rossignol and E. Gengembre, Appl. Catal., A, 1999, 182, 317–325.
7 S. Balcon, S. Mary, C. Kappenstein and E. Gengembre, Appl. Catal., A, 2000, 196, 179–190.
8 J. P. Contour and G. Pannetie, J. Catal., 1972, 24, 434–445.
9 Y. K. Alhaydari, J. M. Saleh and M. H. Matloob, J. Phys. Chem., 1985, 89, 3286–3290.
10 A. Haryanto, S. Fernando, N. Murali and S. Adhikari, Energy Fuels, 2005, 19, 2098–2106.
11 P. Stoltze, Phys. Scr., 1987, 36, 824–864.
12 K. Honkala, A. Hellman, I. N. Remediakis, A. Logadottir, A. Carlsson, S. Dahl, C. H. Christensen and J. K. Norskov, Science, 2005, 307, 555–558.
13 A. Hellman, K. Honkala, I. N. Remediakis, A. Logadottir, A. Carlsson, S. Dahl, C. H. Christensen and J. K. Norskov, Surf. Sci., 2006, 600, 4264–4268.
14 A. Hellman, K. Honkala, I. N. Remediakis, A. Logadottir, A. Carlsson, S. Dahl, C. H. Christensen and J. K. Norskov, Surf. Sci., 2009, 603, 1731–1739.
15 C. C. Wang, J. Y. Wu, T. L. M. Pham and J. C. Jiang, ACS Catal., 2014, 4, 639–648.
16 G. Novell-Leruth, J. M. Ricart and J. Perez-Ramirez, J. Phys. Chem. C, 2008, 112, 13554–13562.
17 K. Rasim, M. Bobeth, W. Pompe and N. Seriani, J. Mol. Catal. A: Chem., 2010, 325, 15–24.
18 T. S. Askgaard, J. K. Norskov, C. V. Ovesen and P. Stoltze, J. Catal., 1995, 156, 229–242.
19 J. Greeley and M. Mavrikakis, J. Am. Chem. Soc., 2004, 126, 3910–3919.
20 S. Kandoi, J. Greeley, M. A. Sanchez-Castillo, S. T. Evans, A. A. Gokhale, J. A. Dumesic and M. Mavrikakis, Top. Catal., 2006, 37, 17–28.
21 A. A. Gokhale, S. Kandoi, J. P. Greeley, M. Mavrikakis and J. A. Dumesic, Chem. Eng. Sci., 2004, 59, 4679–4691.
22 C. Stegelmann, N. C. Schiodt, C. T. Campbell and P. Stoltze, J. Catal., 2004, 221, 630–649.
23 A. A. Gokhale, J. A. Dumesic and M. Mavrikakis, J. Am. Chem. Soc., 2008, 130, 1402–1414.
24 L. C. Grabow, A. A. Gokhale, S. T. Evans, J. A. Dumesic and M. Mavrikakis, J. Phys. Chem. C, 2008, 112, 4608–4617.
25 R. J. Madon, D. Braden, S. Kandoi, P. Nagel, M. Mavrikakis and J. A. Dumesic, J. Catal., 2011, 281, 1–11.

26 A. Rold´an, G. Novell, J. M. Ricart and F. Illas, J. Phys. Chem. C, 2010, 114, 5101–5106.

27 N. Y. Dzade, A. Roldan and N. H. de Leeuw, J. Chem. Phys., 2013, 139, 124708–124708.

28 S. S. Tafreshi, A. Roldan and N. H. de Leeuw, Phys. Chem. Chem. Phys., 2015, 17, 21533–21546.

29 H. Eyring, J. Chem. Phys., 1935, 3, 107–115.

30 M. G. Evans and M. Polanyi, Trans. Faraday Soc., 1935, 31, 0875–0893.

32 J. Pineda and S. D. Schwartz, Philos. Trans. R. Soc., B, 2006, 361, 1433–1438.

31 D. S. Sholl and J. A. Steckel, Density functional theory: a practical introduction, Wiley, Hoboken, N.J., 2009.

33 E. V. Anslyn and D. A. Doughtery, Transition State Theory and Related Topics, Modern Physical Organic Chemistry, University Science Books, 2006.

34 S. S. Tafreshi, A. Roldan, N. Y. Dzade and N. H. de Leeuw, Surf. Sci., 2014, 622, 1–8.

35 S. S. Tafreshi, A. Roldan and N. H. de Leeuw, J. Phys. Chem. C, 2014, 118, 26103–26114.

36 S. S. Tafreshi, A. Roldan and N. H. de Leeuw, Surf. Sci., 2015, 637–638, 140–148.

37 G. Kresse and J. Furthmuller, Phys. Rev. B, 1996, 54, 11169–11186.

38 G. Kresse and J. Furthmuller, Comput. Mater. Sci., 1996, 6, 15–50.

39 G. Kresse and J. Hafner, Phys. Rev. B, 1993, 47, 558–561.

42 G. Kresse and D. Joubert, Phys. Rev. B, 1999, 59, 1758–1775.

40 G. Kresse and J. Hafner, Phys. Rev. B, 1994, 49, 14251–14269.

41 J. P. Perdew, K. Burke and M. Ernzerhof, Phys. Rev. Lett., 1996, 77, 3865–3868.

43 P. E. Blochl, Phys. Rev. B, 1994, 50, 17953–17979.

44 S. Grimme, J. Comput. Chem., 2006, 27, 1787–1799.

117, 3949–3957.

45 S. Irrera, A. Roldan, G. Portalone and N. H. De Leeuw, J. Phys. Chem. C, 2013,

46 H. J. Monkhorst and J. D. Pack, Phys. Rev. B, 1976, 13, 5188–5192.

47 R. Koitz, A. P. Seitsonen, M. Iannuzzi and J. Hutter, Nanoscale, 2013, 5, 5589–5595.

48 M. Gajdos and J. Hafner, Surf. Sci., 2005, 590, 117–126.

49 G. Mills and H. Jonsson, Phys. Rev. Lett., 1994, 72, 1124–1127.

50 G. Mills, H. Jonsson and G. K. Schenter, Surf. Sci., 1995, 324, 305–337.

51 A. Heyden, A. T. Bell and F. J. Keil, J. Chem. Phys., 2005, 123, 224101–224115.

52 L. R. Danielson, M. J. Dresser, E. E. Donaldson and J. T. Dickinson, Surf. Sci., 1978, 71, 599–614.

53 F. Bozso, G. Ertl, M. Grunze and M. Weiss, J. Catal., 1977, 49, 18–41.

54 G. Anger, A. Winkler and K. D. Rendulic, Surf. Sci., 1989, 220, 1–17.

55 J. Prasad and J. L. Gland, Langmuir, 1991, 7, 722–726.

56 I. Hussla, H. Seki, T. J. Chuang, Z. W. Gortel, H. J. Kreuzer and P. Piercy, Phys. Rev. B, 1985, 32, 3489–3501.

57 A. Marmier, C. Ramseyer, P. N. M. Hoang, C. Girardet, J. Goerge, P. Zeppenfeld, M. Buchel, R. David and G. Comsa, Surf. Sci., 1997, 383, 321–339.

58 M. J. Sandoval and A. T. Bell, J. Catal., 1993, 144, 227–237.

59 P. B. Rasmussen, P. M. Holmblad, H. Christoffersen, P. A. Taylor and I. Chorkendorff, Surf. Sci., 1993, 287, 79–83.

60 J. M. Campbell and C. T. Campbell, Surf. Sci., 1991, 259, 1–17.

61 C. T. Rettner, D. J. Auerbach and H. A. Michelsen, Phys. Rev. Lett., 1992, 68, 2547–2550.
62 B. E. Hayden, D. Lackey and J. Schott, Surf. Sci., 1990, 239, 119–126.
63 C. Astaldi, A. Bianco, S. Modesti and E. Tosatti, Phys. Rev. Lett., 1992, 68, 90–93.
64 J. Harris, Surf. Sci., 1989, 221, 335–345.
65 J. L. Gland, G. B. Fisher and G. E. Mitchell, Chem. Phys. Lett., 1985, 119, 89–92.
66 J. Prasad and J. L. Gland, Langmuir, 1991, 7, 722–726.
67 J. L. Falconer and H. Wise, J. Catal., 1976, 43, 220–233.
70 B. J. Wood and H. Wise, J. Catal., 1975, 39, 471–480.
68 H. Rauscher, K. L. Kostov and D. Menzel, Chem. Phys., 1993, 177, 473–496.
69 W. M. Daniel and J. M. White, Surf. Sci., 1986, 171, 289–302.
71 R. C. Cosser and F. C. Tompkins, Trans. Faraday Soc., 1971, 67, 526–544.
72 R. C. A. Contaminard and F. C. Tompkins, Trans. Faraday Soc., 1971, 67, 545–555.